

Cite this: *J. Mater. Chem. A*, 2014, 2, 20105

Graphene oxide as dual functional interface modifier for improving wettability and retarding recombination in hybrid perovskite solar cells†

Wenzhe Li, Haopeng Dong, Xudong Guo, Nan Li, Jiangwei Li, Guangda Niu and Liduo Wang*

The interface between perovskite and the hole transport layer (HTL) is sensitive to photoelectric conversion properties. However, this study shows that the interface wettability of the HTL solution on a perovskite surface could be improved. To address this problem, graphene oxide (GO) with amphiphilic function was used to form a buffer layer between the perovskite and the HTL. After the GO modification, the contact angles of the HTL solution on the perovskite film decreased to zero degrees. X-ray photoelectron spectroscopy revealed that the GO interacts with the perovskite by forming Pb–O bonds, and Raman spectroscopy analysis revealed that the two-dimensional carbon–carbon bonds absorbed the hole transport material, 2,29,7,79-tetrakis-(*N,N*-di-*p*-methoxyphenyl-amine)-9,99-spirobifluorene (Spiro-MeOTAD) via π – π interactions. The GO layer improved the contact between the perovskite and HTL, resulting in an enhancement of the short circuit current (J_{SC}). Moreover, using GO as an insulating buffer layer can retard charge recombination in solar cells, as revealed by EIS measured in dark conditions, leading to a significant increase in the open-circuit voltage (V_{OC}) and the fill factor (FF). Consequently, the corresponding average efficiency greatly increased by 45.5%, from 10.0% to 14.5%. Therefore, application of GO as a dual-functional buffer layer on the perovskite layer is a useful strategy for preparing highly efficient hybrid perovskite solar cells.

Received 30th September 2014
Accepted 15th October 2014

DOI: 10.1039/c4ta05196c

www.rsc.org/MaterialsA

1 Introduction

Organic–inorganic-hybrid materials, such as perovskite $\text{CH}_3\text{NH}_3\text{PbI}_3$, have been used as light harvesters for solar cells because of their multiple capabilities of light absorption, charge separation, and transport of both holes and electrons.^{1–7} The additional advantages of low cost, easy fabrication, and high efficiency mean solar cells based on this type of material are potentially ideal photoelectric devices.^{1,8} The efficiency of lead halide perovskite ($\text{CH}_3\text{NH}_3\text{PbX}_3$, X = Cl, Br, I)-based photovoltaic devices has taken a huge leap forward from 3.8% to more than 19% in just 5 years.^{7,9,10} Compared with vacuum deposition⁴ and vapor-assisted solution processing,¹¹ the sequential deposition method has the advantages of easy control and good repeatability, and can improve the loading of PbI_2 with a $\text{PbI}_2/\text{N,N}$ -dimethylformamide (DMF) solution. Using this method, more densely packed and smooth $\text{CH}_3\text{NH}_3\text{PbI}_3$ crystals on TiO_2 films have been obtained,¹² as well as the highest process cycle efficiency (PCE) of as-prepared dye-sensitized solar cells (up to

15%), with a long-term stability maintaining 80% of the initial PCE after 500 h.⁶ The hole transport material (HTM) 2,29,7,79-tetrakis-(*N,N*-di-*p*-methoxyphenyl-amine)-9,99-spirobifluorene (Spiro-MeOTAD) has commonly been used, with 4-*tert*-butylpyridine (TBP) and bis(trifluoromethane)sulfonimide lithium salt (Li-TFSI) as additives.¹³

Graphene oxide (GO) is a precursor for graphene synthesis by either chemical or thermal reduction methods.^{14,15} Graphene oxide has attracted a great deal of attention because of its reliability and low production costs, large-scale production capability, and good dispersibility in many solvents.^{16–18} With respect to structure, GO presents a two-dimensional carbon–carbon structure encompassing various oxygen-containing functional groups, mostly in the form of carboxyl, carbonyl, phenol, lactone, and quinone typically at the sheet edges.^{14,19} This structure provides flexibility for guiding modification of GO sheets via covalent functionalization.¹⁸ The hydrophilic edges and hydrophobic centers of the GO sheets cause them to act as surfactants.²⁰ However, the oxygen functional groups in GO create structural inhomogeneities, including reduced electron mobility, which make it a potential material for retarding electron recombination in perovskite solar cells, offering an alternative to materials we have previously explored for interface engineering, such as Al_2O_3 (ref. 21 and 22) and montmorillonite (MMT).²³

Key Lab of Organic Optoelectronics & Molecular Engineering of Ministry of Education, Department of Chemistry, Tsinghua University, Beijing 100084, China. E-mail: chldwang@mail.tsinghua.edu.cn; Fax: +86 10 62795137; Tel: +86 10 62788802

† Electronic supplementary information (ESI) available. See DOI: 10.1039/c4ta05196c

Herein, we demonstrate that the interface between the HTL solution and perovskite cannot have perfect wettability, but that GO as an amphiphilic functional layer treating the perovskite surface decreases the contact angles (CAs) to zero degrees. The reaction of the GO to perovskite was studied by X-ray photoelectron spectroscopy (XPS), and the reaction of GO to Spiro-MeOTAD in the HTL was investigated by infrared (IR) and Raman spectra. The PCE of the fabricated devices treated with GO is enhanced significantly. Electrochemical impedance spectroscopy (EIS) measurements in sunlight reveal a decrease in the forward transport resistance, which enhances wettability, and the increase of the charge collection efficiency results in higher short circuit current (J_{sc}) values. EIS measurements in the dark were used to study the behavior of electron recombination at the TiO_2 /sensitizer/HTL interface, to examine the increase in the open-circuit voltage (V_{oc}) and the fill factor (FF) in the photocurrent-voltage (J - V) curves.

2 Experimental section

2.1 Solar cell fabrication and GO treatment

TiO_2 compact layers were deposited on fluorine-doped tin oxide glass using atomic layer deposition (Beneq TFS 200). Titanium dioxide (TiO_2) was deposited at 150°C using titanium tetrachloride (TiCl_4) and H_2O as Ti and O precursors, respectively, in pulse mode in a nitrogen flow of 300 sccm. The TiCl_4 was retained in the chamber for 0.25 s, and subsequently the H_2O was retained for 0.25 s. The wait period for both precursors was 1 s. At 150°C , the TiO_2 growth rate per cycle was 0.5 \AA , and TiO_2 deposition was performed for 300 cycles to achieve a layer thickness of 17 nm. Nanocrystalline TiO_2 paste (18NRT from Dyesol Company; diluted to w/w 33%) was deposited on the pre-treated fluorine-doped tin oxide substrate at 7000 rpm for 30 s, followed by heating at 500°C for 1 h. The thickness of the annealed TiO_2 films was nearly 350 nm, as determined by scanning electron microscopy (SEM; JEOL JSM-7401F). The perovskite preparation process followed ref. 6. DMF (Aldrich, 99.9%) solution (462 mg mL^{-1}) containing PbI_2 (Aldrich, 99.9985%) was heated to 60°C under magnetic stirring overnight, whereupon the mixture was spin coated on the as-prepared TiO_2 film at 6500 rpm for 90 s in a glove box. The films were then dried at 70°C for 30 min and dipped in a solution of $\text{CH}_3\text{NH}_3\text{I}$ in 2-propanol (10 mg mL^{-1}) for 120 s and then rinsed with 2-propanol. The films were dried at 70°C for 30 min, after which the color of the films was dark red. The GO (JCGO-99-1-100n; JCNANO company) dispersion was prepared by mixing 3 mg of GO powder with 1 mL chlorobenzene, *via* shaking for 2 min and filtering with a 220 nm filter. The final concentration of the solution was 340 mg L^{-1} at full dilution. After a perovskite annealing process, diluted GO dispersion (85 mg L^{-1}) was dripped on perovskite film followed by 30 s infiltration, then this was spin coated at 7000 rpm for 30 s. The control sample was treated by chlorobenzene using the same process. Thirty minutes later, the $\text{CH}_3\text{NH}_3\text{PbI}_3$ -coated TiO_2 films were covered with the HTM solution using spin coating at 4000 rpm for 30 s. The HTM composition was 73 mg of Spiro-MeOTAD, 9.1 mg of Li-TFSI, and $37.5\text{ }\mu\text{L}$ of TBP (96%, Aldrich) in a solvent

consisting of 1 mL of chlorobenzene (99.8% SuperDry, J&K Scientific). For the counter electrode, a 60 nm-thick film of Au was deposited on top of the HTL overlayer by thermal evaporation.

2.2 Characterization

Ultraviolet-visible light absorption spectra were employed to assess the absorption properties of the perovskite-sensitized TiO_2 film with a Hitachi U-3010 spectroscope. The CAs were measured with an optical CA meter (OCA20, Dataphysics) at room temperature. The Raman spectra were collected using a Raman spectrometer (Renishaw) with a 514 nm laser, and XPS was measured with a PHI 5300 ESCA PerkinElmer spectrometer. Topographical and potential phase maps were measured under ambient air with a Kelvin probe force microscope (Seiko instrument SPA 400). The Fourier transform infrared (FTIR) spectrum was measured with a PerkinElmer Spectrum GX FTIR spectrometer. The photocurrent-voltage (J - V), incident photon-to-electron conversion efficiency (IPCE), and electrochemical impedance spectra (EIS; from 0.1 to 10^5 Hz) were measured using an electrochemical workstation (ZAHNER CIMPS, Germany) under a solar simulator (Xenon lamp, Oriel, AM 1.5, 100 mW cm^{-2}). The mask active area was fixed at 0.09 cm^2 .

3 Results and discussion

3.1 GO influence on the interface wettability between HTL solution/perovskite

At the perovskite and HTL interface, the HTL solution, including Spiro-MeOTAD, Li-TFSI, TBP, and chlorobenzene, cannot immediately spread out; the CAs of the HTL solution directly on the perovskite film were measured and found to be 13.4° (Fig. 1a). The perovskite $\text{CH}_3\text{NH}_3\text{PbI}_3$ material has a strong polarity, whereas the polarity of the HTL containing the chlorobenzene solvent is weaker. CAs can be determined on substrates of different polarities and roughness,²⁴ but the perovskite surface is unfortunately quite rough, with a calculated root mean square roughness value of 44.3 nm .²⁵ Additionally, the TBP in the HTL is helpful in reducing the surface tension, although our previous studies have found that TBP in the HTL can corrode and fade the perovskite films. To improve the HTL solution wettability, a type of lamellar surfactant is

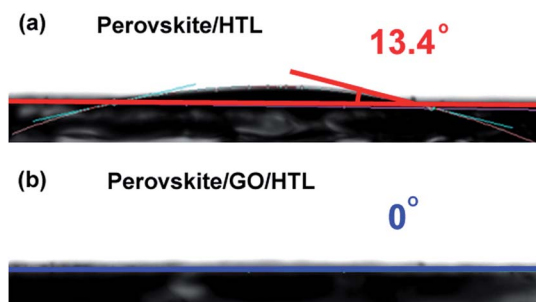


Fig. 1 HTL solution contact angles of perovskite films (a) w/o and (b) with GO modification on a FTO substrate.

needed to enhance the interface contact between the perovskite and HTL. Graphene oxide is an amphiphilic material, where the main surface of the sheet contains polyaromatic rings and the edge of the sheet concentrates oxygen atoms into carboxylic acid groups.²⁶ Therefore, a monolayer GO sheet dispersed in chlorobenzene is spin coated onto the perovskite and the HTL solution is subsequently dropped onto this modified surface, whereupon the contact angle decreases to zero degrees. Consequently, the GO on the perovskite effectively improves the ability of the HTL to spread, which would benefit the contact between perovskite and HTL.

3.2 The interaction between GO and perovskite/HTL

3.2.1 The interaction between GO and perovskite. XPS spectra of the signals for I 3d, O 1s, C 1s, and Pb 4f were collected from the perovskite films, GO powders, and GO-modified perovskite films to probe the chemical environment of the elements in the near-surface range (Fig. 2a). The perovskite films without and with GO modification exhibit an increased

atomic ratio of Pb : C : O, increasing from 1 : 1.78 : 0.39 to 1 : 5.57 : 1.64, respectively. Because GO is composed mainly of C and O, the increase in C and O contents is because of the GO present on perovskite. As indicated in Fig. 2b, the asymmetric and broad features of the observed C 1s peaks suggest the co-existence of distinguishable models. In the perovskite spectra, the main peak located at 286.13 eV is attributed to the C–N binding energy. Deconvolution core level spectra at 284.84, 286.87, and 288.74 eV are in agreement with the GO data.²⁷ The sharp peak located at 284.84 eV is attributed to sp^2 hybridized carbon atoms,²⁸ the peak at 286.87 eV is ascribed to the existence of C–OH bonds,²⁹ and the weak peak at 288.74 eV is ascribed to the existence of C–OOH bonds.³⁰ Compared with the spectra of unmodified films, the intensity of the peak at 284.82 eV improves significantly for GO-modified perovskite films, and the content ratio of the C–C to C–N bonds increases from 0.18 to 1.00 when the GO surface is modified. Fig. 2c shows the high-resolution spectra of O 1s. In the case of the perovskite films, the curve fitting of the O 1s spectrum basically indicates a trace amount of the O element. For GO powders, the O 1s spectra indicate two components centered at 532.62 and 535.74 eV, which are commonly ascribed to the surface oxygen complexes of the carbon phase.^{31,32} For the GO-modified film, the three peaks at 533.48, 532.27, and 530.4 eV clearly improve, where the peak at 533.48 eV is ascribed to absorbed water vapor,³³ and the peak with higher intensity at 532.27 eV is attributed to organic oxide contribution. The lead–oxygen bonds in pure PbO are located at 528.9 eV,³⁴ but when the carboxyl groups connect with organic groups, such as the O in GO, the peak shifts to higher binding energies because of the electron distinct effect.³⁵ Therefore, the strength increase of the peak at 530.4 eV is most likely caused by creation of Pb–O bonds.

High-resolution spectra of Pb 4f are shown in Fig. 2d, and prove that GO decreases the defects in perovskite. In the perovskite case, the relatively weak peak is at 136.74 eV, and is associated with Pb possessing a low state of unsaturated atoms.³⁶ The reason for unsaturated Pb atoms in perovskite is I atoms vacancy. The vacancy results in ionization of the point defects, which is of importance for surpassing charge transport and creating luminescent centers.^{37,38} The literature reports that defects can be surpassed by iodopentafluorobenzene,³⁹ thiophene, and pyridine.⁴⁰ On one hand, the defects in crystal affect the charge separating and transport. On the other, the defects in the crystal state decrease the thermodynamic stability. After GO surface modification, the ratio of the areas of the peaks at 136.74 and 138.22 eV decreases from 6.79×10^{-2} to 3.57×10^{-2} . Combining this result with the information from the O 1s curves, it is evident that parts of the O atoms in the GO connect with unsaturated Pb atoms in the perovskite, surpassing the surface defect states.

Kelvin probe force microscopy was used to detect the potential difference of a perovskite surface prepared on a silicon base. Fig. 3 reveals the topographical and potential phase of the samples with and without GO dispersions. The oxygen functional groups in GO create structural inhomogeneities, including reduced electron mobility.^{41,42} Fig. 3b and d shows that the potential differences at the perovskite surface

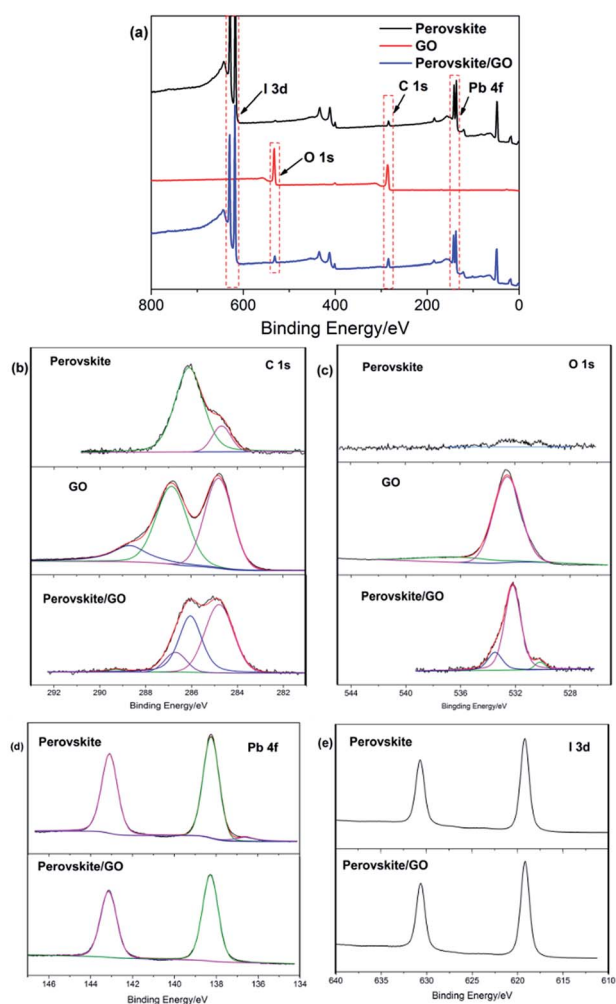


Fig. 2 The overview (a) and the corresponding high-resolution XPS spectra (b) C 1s, (c) O 1s, (d) Pb 4f, and (e) I 3d of the as-prepared perovskite films, GO powder, and GO modified perovskite films.

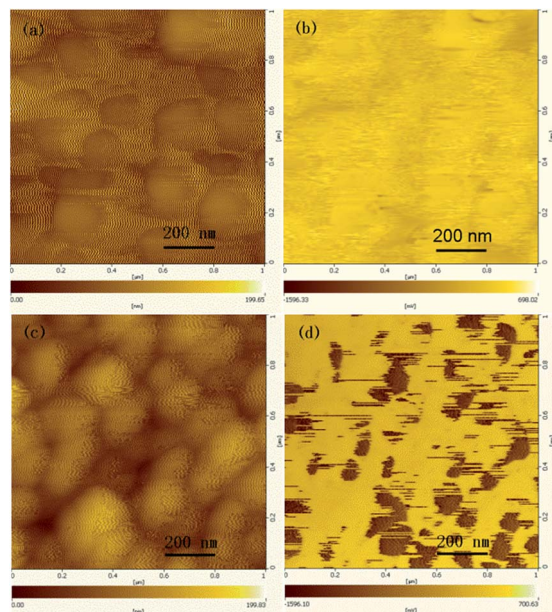


Fig. 3 KPFM images of (a) TOPO phase and (b) potential phase of Si slice covered by perovskite, (c) TOPO phase and (d) potential phase of Si slice covered by perovskite with GO.

significantly increase when GO is added, where the regions in Fig. 3d with dark colors correspond to regions of lower potential covered by GO sheets. Furthermore, the dispersion and morphology of these regions of lower potential closely follow the GO area size of approximately 150 nm. These results together with the XPS results lead us to conclude that GO partially covers the perovskite.

3.2.2 The interaction between GO and HTL. To confirm the reaction between GO and the HTM Spiro-MeOTAD, 2 mg of Spiro-MeOTAD was mixed with 5 mg of GO powder in chlorobenzene and the mixture was centrifuged and dispersed for five cycles to remove free Spiro-MeOTAD. After vacuum drying at 60 °C for 24 h, brown-colored powders were obtained. The IR spectra obtained from the GO powders and the Spiro-MeOTAD-treated GO powders are shown in Fig. 4a. It is clear that there is improvement in the absorbance in the range of 500–2000 cm^{-1} after Spiro-MeOTAD treatment. The peaks at 1602, 1498, 1466, and 1248 cm^{-1} , especially, indicate absorption of methoxy phenyl, which connects to the molecular periphery of Spiro-

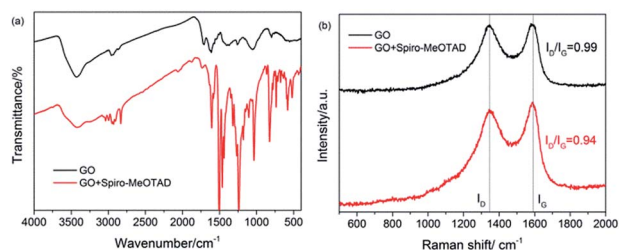


Fig. 4 (a) IR spectra and (b) Raman spectra of GO and GO/Spiro-MeOTAD samples.

MeOTAD, and the GO performs as a base absorbing the Spiro-MeOTAD onto its surface.

The chemical reaction of GO with Spiro-MeOTAD is further supported by the Raman spectra shown in Fig. 4b. The Raman spectra of the GO show two distinct and broad peaks at 1350 and 1580 cm^{-1} . The peak at 1350 cm^{-1} is usually associated with the sp^3 bonding in GO, while the peak at 1580 cm^{-1} is usually related to the sp^2 bonding, and both are recognized as I_D and I_G , respectively. The curves show a slight decrease in the ratio of the I_D to I_G band intensity from 0.99 to 0.94 after Spiro-MeOTAD treatment. This may be because of the increased influence of the π - π interaction on the molecule, which thereby enhances the interactions between the GO layers and the Spiro-MeOTAD molecule and decreases the distortion of the GO.

3.3 Photovoltage performance of perovskite solar cells after adding GO as a buffer

Solid-state perovskite solar cells were fabricated using the GO as a buffer between the perovskite absorption layer and the HTL, and the subsequent enhancement of the device conversion efficiency was investigated. The J - V curves were measured with a 0.2 s delay after each 10 mV voltage step (50 mV s^{-1}). The scans carried out in negative directions from 1.1 V to 0 V followed the method provided in ref. 43. The content of the GO dispersion was optimized from 0 to 340 mg L^{-1} , and the V_{OC} , J_{SC} , FF, and

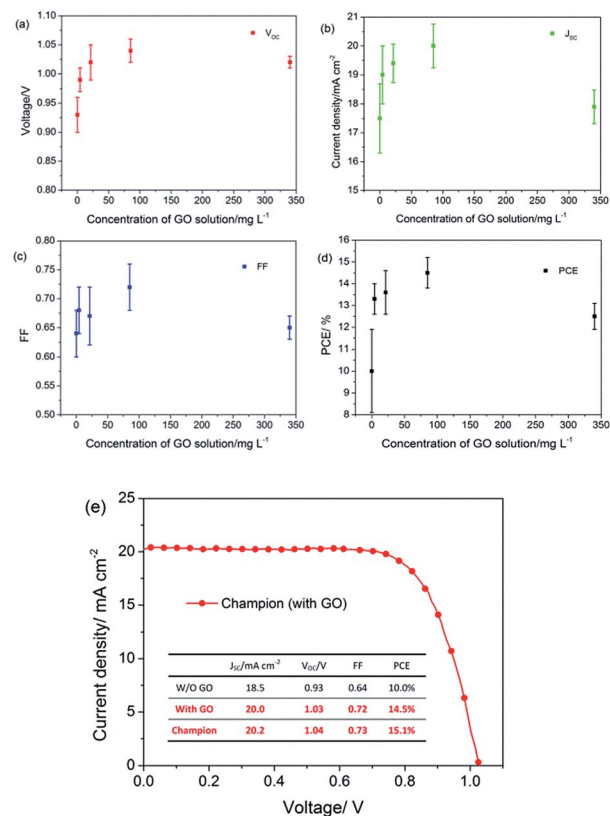


Fig. 5 (a) V_{OC} , (b) J_{SC} , (c) FF, and (d) PCE data followed the content of GO dispersion from 0 to 340 mg L^{-1} . (e) The J - V characteristics of devices with GO addition; the inset shows the parameter of the cells.

PCE values *via* calculating results from 24 devices for each GO content point are shown in Fig. 5. The results show that the optimum content of GO is 85 mg L^{-1} , and this optimum GO content is used to cover the perovskite as a buffer layer. The device with GO performs better, with the average PCE increasing by 45.5% from 10.0% to 14.5%, and all of the V_{OC} , J_{SC} , and FF values increasing. The champion cells for 15.1% efficiency are best performed in the 24 devices with the same preparation conditions. The addition of a GO layer before the HTL thus improves the efficiency of the perovskite-sensitized all-solid-state solar cells.

3.3.1 Effect on J_{SC} enhancement after adding GO as a buffer. Under full illumination, the Nyquist plot (Fig. 6a) shows the typical semicircles in a frequency range of 1–100 kHz with 0.9 V DC bias. The spectra show the first arc at high frequency and second arc with low frequency, because the GO sheet can enhance the contact between perovskite and HTL as previously discussed. The first arc is related to selective contact,^{44,45} which is decreased with GO addition. The electron-selective contact is not changed, therefore the hole-selective contact enhances with GO addition. This may be because of improvement of the interface wettability by the GO layer, which is supported by the contact angle results, and reducing the gap between the rough perovskite and the HTL. The improved contact in the post-perovskite interface can also increase the FF in device performance.⁴⁶

Monochromatic, incident photon-to-electron conversion efficiency (IPCE) of the device maintains a similar magnitude for the wavelength range of 400–800 nm, matching the absorbance range of perovskite. The IPCE can be expressed by⁴⁷

$$\text{IPCE}(\lambda) = \text{LHE}(\lambda)\phi_{\text{inj}}\eta_c \quad (1)$$

where LHE is the light-harvesting efficiency, ϕ_{inj} is the quantum yield of electron injection from the excited sensitizer into the TiO_2 conduction band, and η_c is the collection efficiency of the photo-generated charge carriers. We examined the three efficiency parameters in eqn (1) separately to elucidate the reasons for the higher IPCE values. The light absorption of the TiO_2 /perovskite film, which is related to the LHE value, slightly increases with the addition of GO (Fig. S1†). However, the large IPCE value enhancements, such as the 20.1% enhancement at the 700 nm wavelength, suggest that there are further influences on the IPCE values. The η_c is determined by the process of

electron collection from TiO_2 to FTO and hole collection from hole transporter to Au counter electrode. The process is not related to GO addition in the interface between perovskite and HTL. The ϕ_{inj} is determined not only by the process of electron injection from perovskite excited state to TiO_2 CB, but also the hole injection to hole transporter. The GO addition does not influence the electron injection, but the hole injection. The GO enhances the hole-selective contact. Therefore, the hole injection process is improved resulting in enhancement of IPCE and current density.

3.3.2 Effect on recombination retardation after adding GO.

In this study, we notice that GO not only forms an active surface layer connecting the perovskite and HTL, thereby enhancing hole-selective contact, but it also retards the charge recombination occurring at the TiO_2 interface. What is actually happening is that the oxygen functional groups in GO break the homogeneities of the graphene, causing reduced electron mobility.^{41,42} Therefore, GO as an insulator⁴⁸ and defect-surpassing agent may function to retard electron recombination at the post-surface of perovskite and HTL. The Nyquist plot of the impedance spectra was acquired in dark condition, and the spectra were obtained for 0.9 V DC bias in a frequency range of 0.1–100 kHz (Fig. 7a). In the equivalent circuit model, R_1 is related to recombination resistance and CPE_1 is the chemical capacitance of the film; R_2 and CPE_2 are related to HTM resistance, capacitance, and the extraction in the Au electrode. The first arc at higher frequencies is related to the HTM transport and extraction in the Au electrode. The main arc is caused by a combination of the recombination resistance (R_2) and the chemical capacitance of the film (CPE_2).^{45,49–51} The R_1 values change from 596 Ω without GO to 784 Ω with GO, a 31.5% increase. The recombination resistance increase may result from introduction of insulator at the interface and surpassing of perovskite surface defects. Generally, increased resistance in dark conditions indicates a restrained charge recombination. In our case, this was verified by the dark current measurement, in which the J – V curve was recorded from the fabricated device being measured in the dark. As shown in Fig. 6b, there is 1.8 times the amount of dark current found in the unmodified device than in the modified one, for example at $V_{\text{OC}} = 1.0 \text{ V}$.

Changes in the V_{OC} can reveal the extent of delayed electron recombination, so we determined V_{OC} using the formula⁵²

$$V_{\text{OC}} = \left(\frac{mRT}{F} \right) \ln \left(\frac{I_{\text{SC}}}{I_0} - 1 \right) \quad (2)$$

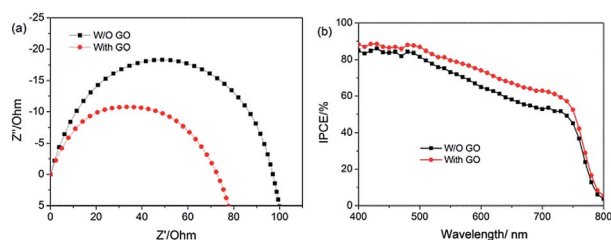


Fig. 6 (a) Nyquist plots under sunlight (1.5 AM) condition without GO buffer and (red) with GO addition to the HTL and (b) IPCE curves of devices.

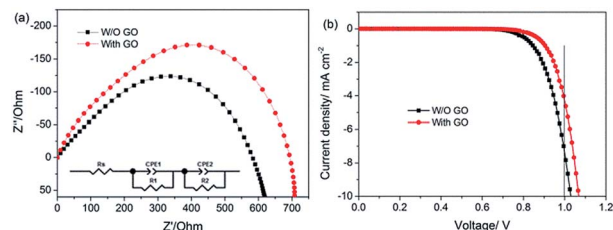


Fig. 7 (a) Nyquist plots under dark condition with 0.9 V bias voltage and (b) the dark current curves.

where I_{SC} is the short-circuit photocurrent, I_0 is the dark current, m is the ideality factor whose value is between 1 and 2 for perovskite solar cells, and R and F are the ideal gas and Faraday constants, respectively. According to eqn (2), V_{OC} increases with decreasing I_0 . Theoretically, the extent of the delayed charge recombination also improves the FF values, which can be determined from the J - V plot analysis, and are consistent with our results.

4 Conclusions

We identified an efficient method to improve the photovoltaic performance of perovskite-sensitized solar cells using GO as an amphiphilic modifier to enhance the interface contact between perovskite and the HTL. After the GO interface treatment, the HTL contact angles on the perovskite films decreased from 13.4 to 0.0 degrees. The interaction between GO and perovskite and HTL was studied to ensure the amphiphilic function. The XPS results reveal that GO interacts with the perovskite by Pb-O bonding, which surpasses the unsaturated Pb bond on the surface. Raman spectroscopy analysis reveals that the two-dimensional carbon-carbon bonds absorb Spiro-MeOTAD by a π - π interaction. The corresponding efficiency of the device is improved by 45.5%, and an overall efficiency of 15.1% is obtained under AM 1.5 sunlight. An increase in J_{SC} is attributed to an enhanced charge collection efficiency resulting from improved contact between the perovskite and HTL. The enhancement of V_{OC} , especially for the FF, benefits from a restrained charge recombination. This is evidenced by the EIS measured in dark conditions, where the recombination resistance is increased in the dark. This work therefore supplies a useful strategy to enhance the efficiency of all-solid-state perovskite solar cells.

Acknowledgements

This work is supported by the National Natural Science Foundation of China under Grant no. 51273104.

Notes and references

- 1 L. Etgar, P. Gao, Z. Xue, Q. Peng, A. K. Chandiran, B. Liu, M. K. Nazeeruddin and M. Grätzel, *J. Am. Chem. Soc.*, 2012, **134**, 17396–17399.
- 2 M. M. Lee, J. Teuscher, T. Miyasaka, T. N. Murakami and H. J. Snaith, *Science*, 2012, **338**, 643–647.
- 3 G. Xing, N. Mathews, S. Sun, S. S. Lim, Y. M. Lam, M. Grätzel, S. Mhaisalkar and T. C. Sum, *Science*, 2013, **342**, 344–347.
- 4 M. Liu, M. B. Johnston and H. J. Snaith, *Nature*, 2013, **501**, 395–398.
- 5 J. H. Heo, S. H. Im, J. H. Noh, T. N. Mandal, C.-S. Lim, J. A. Chang, Y. H. Lee, H.-j. Kim, A. Sarkar, K. NazeeruddinMd, M. Gratzel and S. I. Seok, *Nat. Photonics*, 2013, **7**, 486–491.
- 6 J. Burschka, N. Pellet, S.-J. Moon, R. Humphry-Baker, P. Gao, M. K. Nazeeruddin and M. Gratzel, *Nature*, 2013, **499**, 316–319.
- 7 H. Zhou, Q. Chen, G. Li, S. Luo, T.-b. Song, H.-S. Duan, Z. Hong, J. You, Y. Liu and Y. Yang, *Science*, 2014, **345**, 542–546.
- 8 J. H. Noh, S. H. Im, J. H. Heo, T. N. Mandal and S. I. Seok, *Nano Lett.*, 2013, **13**, 1764–1769.
- 9 A. Kojima, K. Teshima, Y. Shirai and T. Miyasaka, *J. Am. Chem. Soc.*, 2009, **131**, 6050–6051.
- 10 H. J. Snaith, *J. Phys. Chem. Lett.*, 2013, **4**, 3623–3630.
- 11 Q. Chen, H. Zhou, Z. Hong, S. Luo, H.-S. Duan, H.-H. Wang, Y. Liu, G. Li and Y. Yang, *J. Am. Chem. Soc.*, 2013, **136**, 622–625.
- 12 N. Li, H. Dong, H. Dong, J. Li, W. Li, G. Niu, X. Guo, Z. Wu and L. Wang, *J. Mater. Chem. A*, 2014, **2**, 14973–14978.
- 13 T. C. Sum and N. Mathews, *Energy Environ. Sci.*, 2014, **7**, 2518–2534.
- 14 W. S. Hummers and R. E. Offeman, *J. Am. Chem. Soc.*, 1958, **80**, 1339.
- 15 D. R. Dreyer, S. Park, C. W. Bielawski and R. S. Ruoff, *Chem. Soc. Rev.*, 2010, **39**, 228–240.
- 16 L. Gomez De Arco, Y. Zhang, C. W. Schlenker, K. Ryu, M. E. Thompson and C. Zhou, *ACS Nano*, 2010, **4**, 2865–2873.
- 17 H. Hayashi, I. V. Lightcap, M. Tsujimoto, M. Takano, T. Umeyama, P. V. Kamat and H. Imahori, *J. Am. Chem. Soc.*, 2011, **133**, 7684–7687.
- 18 S. K. Das, C. B. Kc and F. D'Souza, *Fullerenes, Nanotubes, Carbon Nanostruct.*, 2013, **22**, 128–137.
- 19 T. Ramanathan, A. A. Abdala, S. Stankovich, D. A. Dikin, M. Herrera Alonso, R. D. Piner, D. H. Adamson, H. C. Schniepp, X. Chen, R. S. Ruoff, S. T. Nguyen, I. A. Aksay, R. K. Prud'Homme and L. C. Brinson, *Nat. Photonics*, 2008, **3**, 327–331.
- 20 N. Withers, *Nat. Chem.*, 2010, **2**, 526.
- 21 W. Z. Li, J. L. Li, L. D. Wang, G. D. Niu, R. Gao and Y. Qiu, *J. Mater. Chem. A*, 2013, **1**, 11735–11740.
- 22 G. D. Niu, W. Z. Li, F. Q. Meng, L. D. Wang, H. P. Dong and Y. Qiu, *J. Mater. Chem. A*, 2014, **2**, 705–710.
- 23 W. Li, H. Dong, L. Wang, N. Li, X. Guo, J. Li and Y. Qiu, *J. Mater. Chem. A*, 2014, **2**, 13587–13592.
- 24 N. Giovambattista, P. G. Debenedetti and P. J. Rossky, *J. Phys. Chem. B*, 2007, **111**, 9581–9587.
- 25 L. Zheng, Y. Ma, S. Chu, S. Wang, B. Qu, L. Xiao, Z. Chen, Q. Gong, Z. Wu and X. Hou, *Nanoscale*, 2014, **6**, 8171–8176.
- 26 J. Kim, L. J. Cote, F. Kim, W. Yuan, K. R. Shull and J. Huang, *J. Am. Chem. Soc.*, 2010, **132**, 8180–8186.
- 27 K. Dai, D. Li, L. Lu, Q. Liu, J. Lv and G. Zhu, *RSC Adv.*, 2014, **4**, 29216–29222.
- 28 R. Bhowmick, S. Rajasekaran, D. Friebel, C. Beasley, L. Jiao, H. Ogasawara, H. Dai, B. Clemens and A. Nilsson, *J. Am. Chem. Soc.*, 2011, **133**, 5580–5586.
- 29 H. Ago, T. Kugler, F. Cacialli, W. R. Salaneck, M. S. P. Shaffer, A. H. Windle and R. H. Friend, *J. Phys. Chem. B*, 1999, **103**, 8116–8121.
- 30 K. Dai, G. Dawson, S. Yang, Z. Chen and L. Lu, *Chem. Eng. J.*, 2012, **191**, 571–578.
- 31 G. Eda, G. Fanchini and M. Chhowalla, *Nat. Photonics*, 2008, **3**, 270–274.

- 32 K. Dai, L. Lu, Q. Liu, G. Zhu, Q. Liu and Z. Liu, *Dalton Trans.*, 2014, **43**, 2202–2210.
- 33 S. Yamamoto, T. Kendelewicz, J. T. Newberg, G. Ketteler, D. E. Starr, E. R. Mysak, K. J. Andersson, H. Ogasawara, H. Bluhm, M. Salmeron, G. E. Brown and A. Nilsson, *J. Phys. Chem. C*, 2010, **114**, 2256–2266.
- 34 S. Södergren, H. Siegbahn, H. Rensmo, H. Lindström, A. Hagfeldt and S.-E. Lindquist, *J. Phys. Chem. B*, 1997, **101**, 3087–3090.
- 35 D. J. Payne, R. G. Egdell, D. S. L. Law, P.-A. Glans, T. Learmonth, K. E. Smith, J. Guo, A. Walsh and G. W. Watson, *J. Mater. Chem.*, 2007, **17**, 267–277.
- 36 J. Baltrusaitis, H. Chen, G. Rubasinghege and V. H. Grassian, *Environ. Sci. Technol.*, 2012, **46**, 12806–12813.
- 37 J. A. Taylor, G. M. Lancaster and J. W. Rabalais, *J. Electron Spectrosc. Relat. Phenom.*, 1978, **13**, 435–444.
- 38 A. Walsh, *J. Phys. Chem. Lett.*, 2010, **1**, 1284–1287.
- 39 A. Abate, M. Saliba, D. J. Hollman, S. D. Stranks, K. Wojciechowski, R. Avolio, G. Grancini, A. Petrozza and H. J. Snaith, *Nano Lett.*, 2014, **14**, 3247–3254.
- 40 N. K. Noel, A. Abate, S. D. Stranks, E. S. Parrott, V. M. Burlakov, A. Goriely and H. J. Snaith, *ACS Nano*, 2014, DOI: 10.1021/nn5036476.
- 41 W.-J. Yin, T. Shi and Y. Yan, *Appl. Phys. Lett.*, 2014, **104**, 063903–063904.
- 42 G. Eda, C. Mattevi, H. Yamaguchi, H. Kim and M. Chhowalla, *J. Phys. Chem. C*, 2009, **113**, 15768–15771.
- 43 E. L. Unger, E. T. Hoke, C. D. Bailie, W. H. Nguyen, A. R. Bowring, T. Heumüller, M. G. Christoforo and M. D. McGehee, *Energy Environ. Sci.*, 2014, **7**, 3690–3698.
- 44 E. J. Juarez-Perez, M. Wußler, F. Fabregat-Santiago, K. Lakus-Wollny, E. Mankel, T. Mayer, W. Jaegermann and I. Mora-Sero, *J. Phys. Chem. Lett.*, 2014, **5**, 680–685.
- 45 H.-S. Kim, I. Mora-Sero, V. Gonzalez-Pedro, F. Fabregat-Santiago, E. J. Juarez-Perez, N.-G. Park and J. Bisquert, *Nat. Commun.*, 2013, **4**, 2242.
- 46 Q. Wang, J.-E. Moser and M. Grätzel, *J. Phys. Chem. B*, 2005, **109**, 14945–14953.
- 47 M. N. Amalina, A. A. E. Najwa, M. H. Abdullah, M. Z. Musa and M. Rusop, *IOP Conf. Ser.: Mater. Sci. Eng.*, 2013, **46**, 012012.
- 48 P. M. Sommeling, B. C. O'Regan, R. R. Haswell, H. J. P. Smit, N. J. Bakker, J. J. T. Smits, J. M. Kroon and J. A. M. van Roosmalen, *J. Phys. Chem. B*, 2006, **110**, 19191–19197.
- 49 S. Lv, L. Han, J. Xiao, L. Zhu, J. Shi, H. Wei, Y. Xu, J. Dong, X. Xu, D. Li, S. Wang, Y. Luo, Q. Meng and X. Li, *Chem. Commun.*, 2014, **50**, 6931–6934.
- 50 J. A. Christians, R. C. M. Fung and P. V. Kamat, *J. Am. Chem. Soc.*, 2013, **136**, 758–764.
- 51 J. You, Z. Hong, Y. Yang, Q. Chen, M. Cai, T.-B. Song, C.-C. Chen, S. Lu, Y. Liu and H. Zhou, *ACS Nano*, 2014, **8**, 1674–1680.
- 52 T. Stergiopoulos, S. Karakostas and P. Falaras, *J. Photochem. Photobiol., A*, 2004, **163**, 331–340.